Lattice symmetry breaking transition and critical size limit for ferroic orders in nanophase $BiFeO_3$

Valeri Petkov [1,*] and Sarvjit Shastri [2]

[1] *Department of Physics, Central Michigan University, Mt. Pleasant, Michigan 48858, USA*

[2] *X-ray Science Division, Advanced Photon Source, Argonne National Laboratory, Argonne, Illinois 60439, USA*

(Received 11 April 2021; revised 5 July 2021; accepted 5 August 2021; published 30 August 2021)

Finite size effects on the ferroic orders in $BiFeO_3$ are studied by atomic pair distribution function analysis and magnetic measurements. While bulk rhombohedral $BiFeO_3$ exhibits ferroelectricity and antiferromagnetism with a cycloidal magnetic moment arrangement leading to zero magnetization and weak magnetoelectric coupling, $BiFeO_3$ nanoparticles with a size smaller than the spin cycloid period of 62 nm preserve their polar rhombohedral structure and develop ferromagnetism, thus exhibiting coexisting polarization and nonzero magnetization that enhances the magnetoelectric coupling. When the nanoparticles become smaller than 17 nm, however, their crystal lattice expands and becomes nonpolar cubic. They also become superparamagnetic and thus simultaneously cease exhibiting both ferroelectricity and ferromagnetism. Our findings shed light on the interaction between the lattice structure and ferroic orders in nanophase perovskites and also provide a rare example of a lattice symmetry breaking phase transition that determines their critical size.

DOI: 10.1103/PhysRevB.104.054121

I. INTRODUCTION

Multiferroic materials are very actively studied because they exhibit interacting ferroelectric and magnetic degrees of freedom that, on principle, allow us to manipulate their electrical polarization with external magnetic field and magnetization with external electric field, opening the door to a number of useful applications [1–9]. Among the known multiferroics, $BiFeO_3$ (BFO) is unique because it exhibits coexisting ferroelectric ($T_c = 1033$ K) and antiferromagnetic ($T_N = 643$ K) orders over a broad temperature range, including room temperature [10–13]. BFO is a rhombohedral (space group $R3c$) perovskite, which is also often described in terms of a hexagonal lattice [14–16]. Contrary to the aristotype cubic perovskite, Fe-oxygen octahedra in BFO are rotated by 13.8 ° in an antiferrodistortive manner about the pseudocubic $\langle 111\rangle_c$ axis (see Fig. 1), which appears as the polar $\langle 111\rangle_r$ and $\langle 111\rangle_h$ in the rhombohedral and hexagonal unit cell, respectively [17,18]. Both Fe and Bi atoms are shifted from their position in the cubic lattice along $\langle 111\rangle_r$ by approximately 0.22 and 0.61 Å, respectively, giving rise to distinct short (1.92 Å) and long (2.15 Å) Fe-O bonding distances. The distances between nearby Bi and oxygen atoms are not unique either and show a broad distribution, ranging about 2.25–3.5 Å [19]. The bonding between Fe^{3+}/Bi^{3+} and O^{2-} is largely ionic. However, it is believed that it also has a partial covalent character, where oxygen atoms are covalently bonded by O p states to both Bi and Fe, providing a link between the A and B sites of the perovskite ABO_3 lattice [20–24]. It is also believed that the ferroelectric polarization in BFO largely originates from the formation of an asymmetric covalent bond between the lone pair of $6s^2$ electrons of Bi atoms and O^{2-} $2p$ orbitals that stabilizes the off-centering displacement of Bi atoms (positive charge) with respect to the oxygen sublattice (negative charge), leading to the emergence of electric dipoles and spontaneous polarization. Notably, because of the antiferrodistortive rotation of oxygen octahedra, the Fe-O-Fe bond angle appears close to 155°. This is important for the magnetic properties of BFO because the Fe-O-Fe bond angle controls the orbital overlap between oxygen and Fe atoms, and therefore the superexchange interaction between the magnetic moments of the latter. The interaction is antiferromagnetic in character and the moments appear ordered in a G-type antiferromagnetic pattern, where they are aligned parallel to each other within the $(111)_c$ atomic planes and antiparallel to each other between the adjacent $(111)_c$ planes. Furthermore, due to the combined effect of exchange and spin-orbit coupling known as Dzyaloshinskii-Moriya (DM) interactions, the moments of nearby Fe ions are also weakly canted away from a perfect antiferromagnetic ordering, resulting in a weak magnetization. However, superimposed on the canting is a long-range magnetic superstructure, featuring a cycloidal spin arrangement with a period of about 62 nm, leading to a cancellation of the magnetization over a single period of the cycloid. The presence of a spin cycloid and zero net magnetization negate any linear magnetoelectric (ME) coupling present between the polarization and magnetization in BFO, which hampers its usage in practical applications [25–29].

A lot of effort has been put into finding an efficient way to suppress the cycloidal spin order and obtain nonzero magnetization without disturbing the ferroelectric order, and thus improve the ME coupling in BFO. It has been found that it can be suppressed by several factors such as (a) an application of external stress or deposition of thin BFO layers on particular substrates, (b) creation of structural modifications by appropriate cationic substitution, and (c) reduction of BFO to dimensions smaller than the period of the spin cycloid

*Corresponding author: petko1vg@cmich.edu

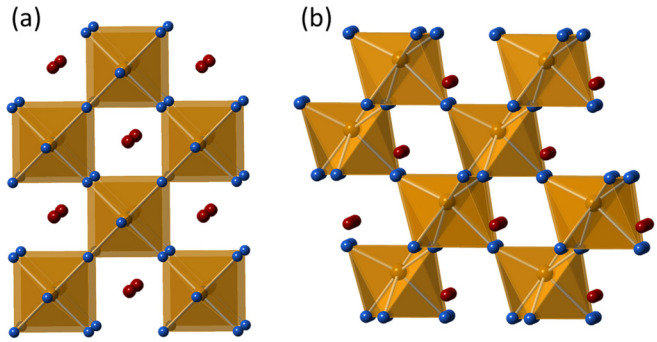

FIG. 1. Fragments from the (a) cubic (space group *Pm*-3*m*) and (b) rhombohedral (space group *R*3*c*) type structures of $BiFeO_3$, as projected down the $\langle 001\rangle_c$ and $\langle 100\rangle_r$ direction of the perovskite lattice, respectively. The structures feature corner shared Fe (brown circles)–oxygen (blue circles) octahedra with Bi (red circles) atoms positioned in the cavities between them. Contrary to the case of cubic $BiFeO_3$, the octahedra in rhombohedral $BiFeO_3$ appear rotated with respect to each other. In addition, because of their relatively small size ($r_{Bi} = 1.17$ Å), Bi atoms in the latter are displaced from the geometrical center of the cavities between the octahedra, rendering the material ferroelectric. In a hypothetical cubic $BiFeO_3$, Bi atoms would not experience such a displacement and the material would appear paraelectric.

[30–33]. The latter approach has been pursued with particular vigor due to the current advancement of nanoscience and technology. Park *et al.* [34] have found that BFO nanoparticles (NPs) exhibit strong magnetic properties that correlate with an increased suppression of the cycloidal spin order with decreasing particle's size. Huang *et al.* [35] found a structural anomaly for BFO particles with a size of approximately 62 nm, which renders them ferromagnetic. In addition, the NPs have been found to exhibit a large ME coupling effect. Sverre *et al.* [36] found that both the rhombohedral distortion characteristic for room-temperature BFO, i.e., intrinsic polarization, and Néel temperature T_N, which scales with the strength of antiferromagnetic-type superexchange interactions, diminish with diminishing the NP size. Based on traditional crystallographic data, the critical size for ferroelectricity has been estimated to be in the order of 9 nm. Carranza-Celis *et al.* [37] have found that BFO NPs show a distorted rhombohedral structure and ferromagneticlike properties at low temperature. They also found that single nanoparticles could exhibit ferroelectricity, thus providing an evidence for the coexistence of ferroelectric and ferromagnetic order in nanosized BFO. However, none of the studies conducted so far has revealed clearly the structural features that stand behind the concurrent evolution of ferroic orders in nanosized BFO. Using high-energy x-ray diffraction (XRD) coupled to atomic pair distribution function (PDF) analysis, we determine the structure of BFO particles with a size ranging 60–5 nm. We also measure their magnetic properties over a broad range of temperatures and magnetic fields. We find that the NPs retain the rhombohedral structure of the bulk state and show an increasingly strong magnetization, i.e., ferromagnetic order, when their size diminishes from 60 nm down to 17 nm. When the NP size is decreased further, Bi atoms suffer large positional disorder resulting in an expansion of the crystal lattice, decreasing its local symmetry to triclinic and increasing its average symmetry to cubic, which is incompatible with ferroelectricity. Concurrently, the ferromagnetic order disappears and the NPs increasingly exhibit superparamagnetic behavior. Thus, the critical size for both ferroelectricity and ferromagnetism in BFO particles appears to be determined by a lattice symmetry breaking transition that takes place when their size is reduced to about 17 nm. The findings improve our knowledge about interactions between lattice, ferroelectric, and ferromagnetic degrees of freedom in physical systems reduced to nanosized dimensions and demonstrate an efficient experimental approach to study them in fine structural detail.

II. EXPERIMENT

Bulk polycrystalline (i.e., μ-sized particles) $BiFeO_3$ was prepared by a traditional solid-state reaction of Bi_2O_3 and Fe_2O_3 at 1100 K. A series of $BiFeO_3$ NPs was prepared by a modified Pechini method using nitrates as metal precursors. Standard XRD, transition electron microscopy, and differential scanning calorimetry studies showed that the particles are single-phase perovskites with a size of 60, 29, 21, 19, 17, 14, 10, and 5 nm. Here we use XRD estimated particle size, which is a measure of the size of domains, or crystallites, coherently scattering x rays. This size is representative of the so-called length of structural coherence, which is critical to the emergence of cooperative properties such as ferroelectricity and magnetism [38]. For reference, an exemplary TEM image of 14 nm BFO particles is given in Fig. S1 in the Supplemental Material (SM) [39]. More details of the NP preparation, purity and particle size determination can be found in Refs. [36,40].

High-energy XRD experiments were conducted at the beamline 1-ID at the Advanced Photon Source, Argonne National Laboratory using x rays with energy of 90.490 keV ($\lambda = 0.1370$ Å). The use of high-energy x rays allows us to reach high wave vectors, which is important for obtaining atomic PDFs with an improved real space resolution. The experimental XRD patterns and respective atomic PDFs are shown in Fig. 2. The PDFs were derived from the XRD data following well-established procedures [41].

Hysteresis loops, shown in Fig. 3, were obtained at room temperature on a PPMS system, varying the magnetic field from −9 to 9 T. Zero-field cooled (ZFC) and field-cooled (FC) magnetization data, shown in Fig. 4, were obtained on the same system over a broad temperature range, extending from 10 to 300 K.

III. EXPERIMENTAL DATA ANALYSIS AND INTERPRETATION

A. X-ray diffraction data

As can be seen in Fig. 2, the XRD pattern for bulk BFO shows sharp Bragg peaks reflecting its good crystallinity. Peaks in the XRD patterns for the NPs increasingly broaden with diminishing NP size and are seen to merge into a few, smeared diffraction features when that size diminishes to 5 nm. Similarly to the Bragg peaks in the respective XRD pattern, peaks in the PDF for bulk BFO appear sharp, indicating the absence of significant local structural disorder. The peaks can be assigned to atomic pair distances known to exist in bulk

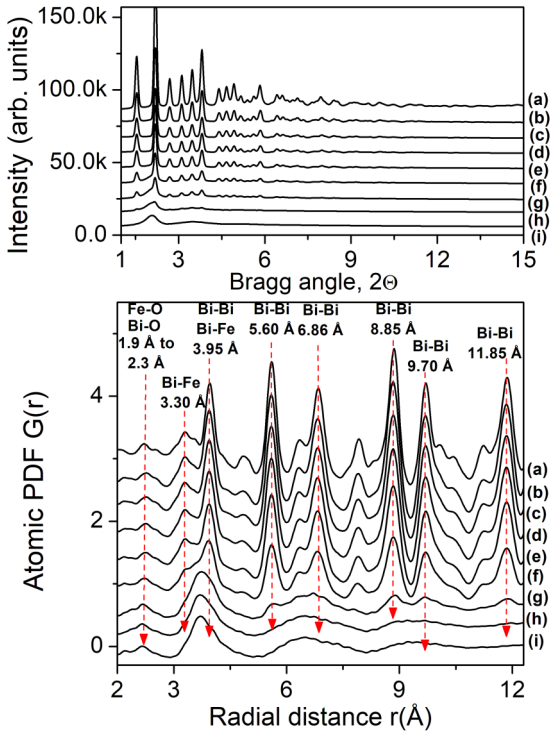

FIG. 2. Upper: Experimental HE-XRD patterns for (a) bulk $BiFeO_3$ and $BiFeO_3$ particles with a size of (b) 60 nm, (c) 29 nm, (d) 21 nm, (e) 19 nm, (f) 17 nm, (g) 14 nm, (h) 10 nm, and (i) 5 nm. Bragg peaks are seen to broaden up with diminishing particle size. Lower: Atomic PDFs derived from the HE-XRD patterns. Several PDF peaks are labeled with the respective atomic pair distances (red arrows). The peaks are seen to broaden and even virtually disappear (e.g., see the PDF peaks at 2.3, 5.6, and 9.7 Å) with diminishing particle size.

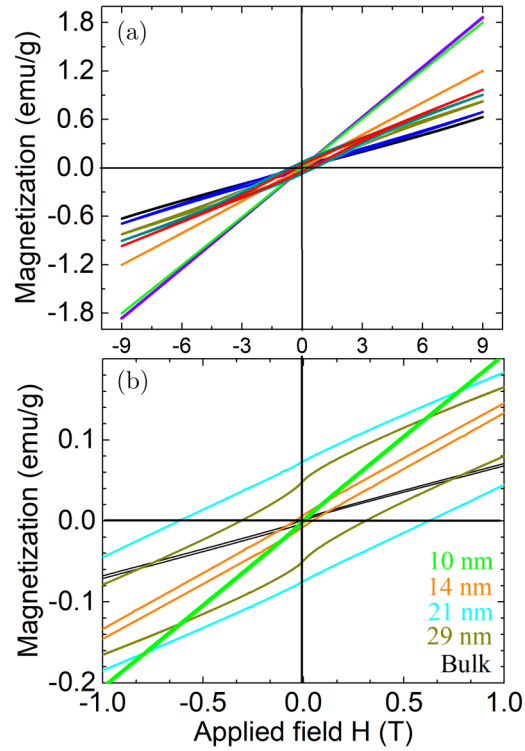

FIG. 3. (a) Room temperature hysteresis (magnetization-field) curves for bulk (black) $BiFeO_3$ and $BiFeO_3$ particles with a size of (blue) 60 nm, (dark yellow) 29 nm, (cyan) 21 nm, (dark cyan) 19 nm, (red) 17 nm, (orange) 14 nm, (green) 10 nm, and (violet) 5 nm. (b) Expanded view of selected hysteresis curves showing the nonlinear evolution of the remnant magnetization (value of M when $H = 0$) and coercive field (value of H when M is zero) with particle size. In particular, the remnant magnetization for 10-nm particles and bulk BFO is zero. As discussed in the text, these materials exhibit superparamagnetic and antiferromagnetic properties, respectively. On the other hand, the remnant magnetization for 21- and 29-nm particles is significant. This is because, as discussed in the text, these particles are ferromagnetic.

BFO. As discussed in Ref. [40], peaks reflecting distances involving Bi atoms broaden fast with diminishing particle size, reflecting the increasing level of positional disorder of Bi atoms.

To ascertain the structure of studied BFO samples, the respective XRD patterns were subjected to Rietveld analysis using the software GSAS II [42]. Results of the analysis are shown in Fig. 5. As can be seen in the figure, the XRD patterns for BFO NPs with a size larger than 17 nm can be well approximated with a structure model based on the well-known rhombohedral (space group $R3c$) structure of bulk BFO. When the rhombohedral structure is described in terms of a hexagonal lattice, the positions of Fe and Bi atoms in the unit cell are $(0, 0, \Delta z(\mathrm{Fe}))$ and $(0, 0, \frac{1}{4} + \Delta z(\mathrm{Bi}))$, respectively, where $\Delta z(\mathrm{Fe})$ and $\Delta z(\mathrm{Bi})$ are the polar displacement of Fe and Bi atoms from their positions in the aristotype cubic (nonpolar) lattice [17–19]. The relative displacement of the cations $\Delta_{\mathrm{rel}} = \Delta z(\mathrm{Bi}) - \Delta z(\mathrm{Fe})$ has been shown to be a good crystallographic measure of the spontaneous polarization in BFO. In particular, it has been shown that the saturation polarization P_s can be evaluated as $P_s = 258(\Delta_{\mathrm{rel}})\,\mu\mathrm{C\,cm^{-2}}$ [43]. From the Rietveld refined lattice parameters and the polar displacements of Fe and Bi atoms summarized in Table S1 in the SM [39], it appears that P_s in bulk BFO would be about $96\,\mu\mathrm{C\,cm^{-2}}$, which is in reasonable agreement with first-principles predictions and recent experimental data for perfect single crystals and thin films [22,44–47].

As can also be seen in Fig. 5, Rietveld fits to the diffuse diffraction patterns for 17, 14, and 5 nm BFO particles are not successful. The failure can be due to the inability of Rietveld method to analyze very diffuse XRD patterns or that of a rhombohedral model to describe the atomic structure of NPs smaller than 19 nm in size, or both. This makes it difficult to judge whether or not they retain the polar structure of bulk BFO and, hence, could harbor ferroelectricity. The difficulty is resolved by atomic PDF analysis, results of which are shown in Figs. 6 and 7. Note that, by definition, the PDF $G(r) = 4\pi r[\rho(r) - \rho_o]$, where $\rho(r)$ is the local and ρ_o is the average atomic number density, respectively. It peaks at all distinct interatomic distances occurring in a material, reflecting its actual atomic structure without assuming any crystal symmetry. Furthermore, while Rietveld analysis concentrates on sharp Bragg peaks in XRD data, an atomic PDF takes into account both the Bragg peaks and the diffuse-type scattering components of XRD data. In this way both the perfect atomic

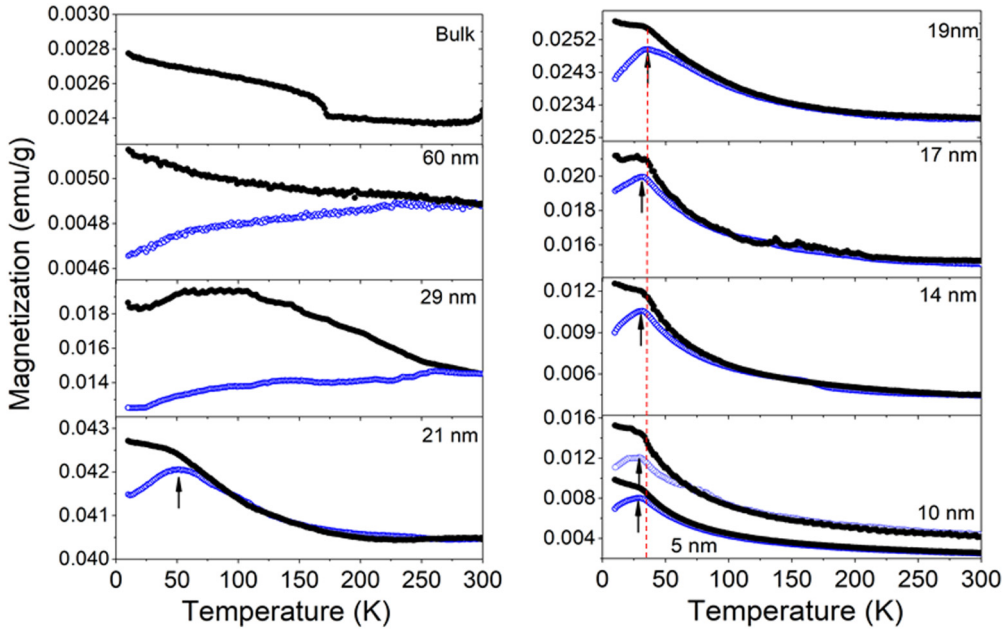

FIG. 4. Zero-field-cooled (blue circles) and 200-Oe field-cooled (black circles) magnetization curves for bulk and nanosized $BiFeO_3$. Arrows (black) mark the blocking temperature T_B for particles with a size smaller than 29 nm. It diminishes with particle's size (see the systematic shift of the position of the arrows from the vertical red line). The kink in the magnetization curve for bulk $BiFeO_3$ seen at about 165 K is attributed to a spin reorientation transition. Broken vertical line (red) is a guide to the eye.

order, manifested in the former, and all local deviations from it, manifested in the latter, are reflected in the experimental PDF data. In this respect, atomic PDF analysis goes beyond traditional techniques for determining the atomic structure of crystals that, typically, reveal well their long-range periodic features alone [48,49].

As can be seen in Figs. 6(a)–6(f), similarly to the respective XRD patterns, the experimental PDFs for BFO NPs larger than 17 nm can be well reproduced by a model based on rhombohedral BFO. The model, however, fails to reproduce the PDF data for 17- and 14-nm particles shown in Figs. 6(g) and 6(h). It cannot reproduce the experimental PDF data for 5 nm either [see Figs. 7(a) and 7(d)]. The result shows clearly that while BFO particles larger than 17 nm exhibit the structure of bulk BFO, those with a smaller size do not. As can be seen in Fig. 7, the low-r part (<15 Å) of the PDFs for the latter can be well reproduced by a distorted rhombohedral model with a triclinic (space group $P1$) symmetry. For reference, such a model has also been found useful in describing the polar structure of bulk BFO [50]. The decrease of the local symmetry from rhombohedral to triclinic in the NPs arises from a near complete loss of structural coherence in the Bi sublattice, as demonstrated by the accelerated decay of Bi-involving atomic pair correlations in the experimental PDF data (see the vertical arrows in Fig. 2) and large, PDF-fit derived root-mean-square displacement (rms) of Bi atoms from their average positions in the undistorted rhombohedral lattice (see Tables S2–S5 [39] and Fig. 8). On the other hand, the higher-r part of these PDFs can be well reproduced by a structure model based on the aristotype cubic (space group $Pm\text{-}3m$) perovskite lattice. Evidently, while BFO particles larger than 17 nm are rhombohedral both locally and on average, those that are 17 nm or smaller in size appear hardly rhombohedral-like, i.e., polar, locally and cubiclike, i.e., nonpolar, on average. As such, the latter may be expected to exhibit limited ferroelectricity, if any. Studies of others indicate that this is exactly how BFO particles with a size smaller than 20 nm behave [51]. Evolution of the unit cell volume and rms displacements of Bi atoms in BFO NPs with their size, as derived from fits to experimental PDF data, are summarized in Fig. 9. Also shown in the figure are average Fe-oxygen-Fe bond angles for the respective NPs. The angles are derived from the refined NP structure data summarized in Tables S2–S5 [39].

B. Magnetization data

As can be seen in Fig. 3(a), and in line with the findings of other studies [35,52–54], the induced magnetization of BFO increases linearly with the applied field, reaching a maximum value of 0.6 emu/g at 9 T. It does not show any hysteresis effects, which is typical for an antiferromagnetic material. The maximum value of the field induced magnetization of BFO NPs increases fast with diminishing their size, reaching a value of about 1.8 emu/g (field of 9 T) for 5-nm particles. Furthermore, as can be seen in Fig. 3(b), BFO particles larger than 17 nm show clear hysteresis loops with nonzero remnant magnetization M_r and coercive field H_c, which is a signature of ferromagnetic order. Both M_r and H_c increase with diminishing particle size and reach their maximum values for 19-nm particles, indicating an increase in the emerged ferromagnetic order. The hysteresis loops, however, collapse back to a single line when the particles size is diminished further, rendering both M_r and H_c virtually zero. The observation indicates that the emerged ferromagnetic order disappears when the size of BFO particles drops below 17 nm. Experimental data for

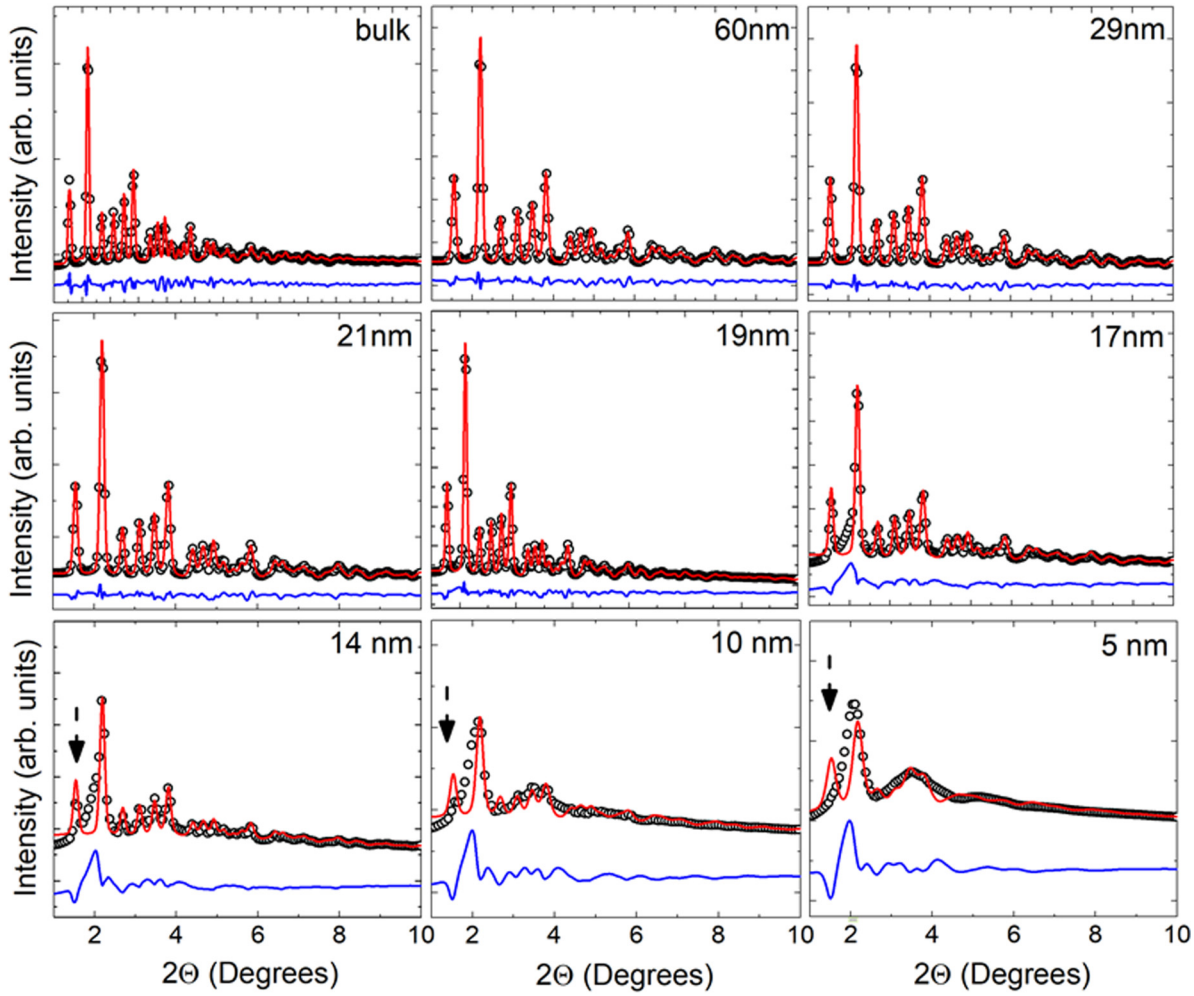

FIG. 5. Rietveld fits (red line) to experimental (symbols) XRD patterns for bulk and nanosized $BiFeO_3$. For clarity, the residual difference (blue line) is shifted downward by subtracting a constant. The fits are based on the rhombohedral (space group $R3c$) type structure exhibited by bulk $BiFeO_3$ at room temperature. The Bragg peaks in the patterns are seen to broaden with diminishing particle's size and merge into broad diffraction features when that size becomes less than 19 nm. The features are difficult to reproduce by Rietveld fits (see the vertical arrows), rendering the values of goodness-of-fit indicators in the order of 15–20%, i.e., unacceptably high. For reference, the goodness-of-fit indicators for bulk $BiFeO_3$ and $BiFeO_3$ particles with a size larger than 17 nm are in the order of 5–10%.

magnetization M_s measured at an external field of 9 T, M_r, and H_c are summarized in Fig. 9.

Inspection of the temperature dependence of the magnetization of bulk BFO, shown in Fig. 4, indicates that the material undergoes a phase transition at about 170 K. Prior studies have attributed the transition to spin reorientation that affects its ferroelectric properties significantly. The ZFC and FC curves for 60 and 29 nm BFO particles do not show this transition but are seen to bifurcate. Usually, the effect arises from the presence of coexisting ferro and antiferromagnetic regions in NPs that may be associated with their surface and core, respectively, and/or magnetic domain pinning effects [55–57]. The ZFC curves for BFO particles smaller than 29 nm develop a broad cusp, which is seen to shift to lower temperature with decreasing particle size further. The cusp can be attributed to magnetic blocking effects induced by the competition between thermal and magnetic anisotropy energy. Large values of M_S, zero M_r, and H_c, and presence of magnetic blocking effects are characteristic signatures of superparamagnetic behavior [53,58,59].

IV. DISCUSSION

In BFO, there is a completion between the antisymmetric DM interactions favoring a canted spin configuration resulting in nonzero magnetization, i.e., favoring a ferromagneticlike state, and symmetric superexchange interactions that favor a completely antiparallel spin configuration and zero magnetization. As a result, a change in the strength of the former would lead to a change in the strength of the latter, and vice versa. In particular, when the size of BFO particles is reduced below 62 nm, the spin cycloid is at least partially destroyed and the magnetization due to spin canting would not anymore cancel to zero, as is the case with bulk BFO. Furthermore, that magnetization would increase with diminishing particle's size further below 62 nm, which is what the experimental data for field-induced magnetization show [see Figs. 3(a) and 9(c)]. The increased magnetization and related stabilization of a ferromagneticlike state would weaken the competing antiferromagnetic state and related superexchange interactions, and thus contribute to the observed decrease in T_N [36,55,60].

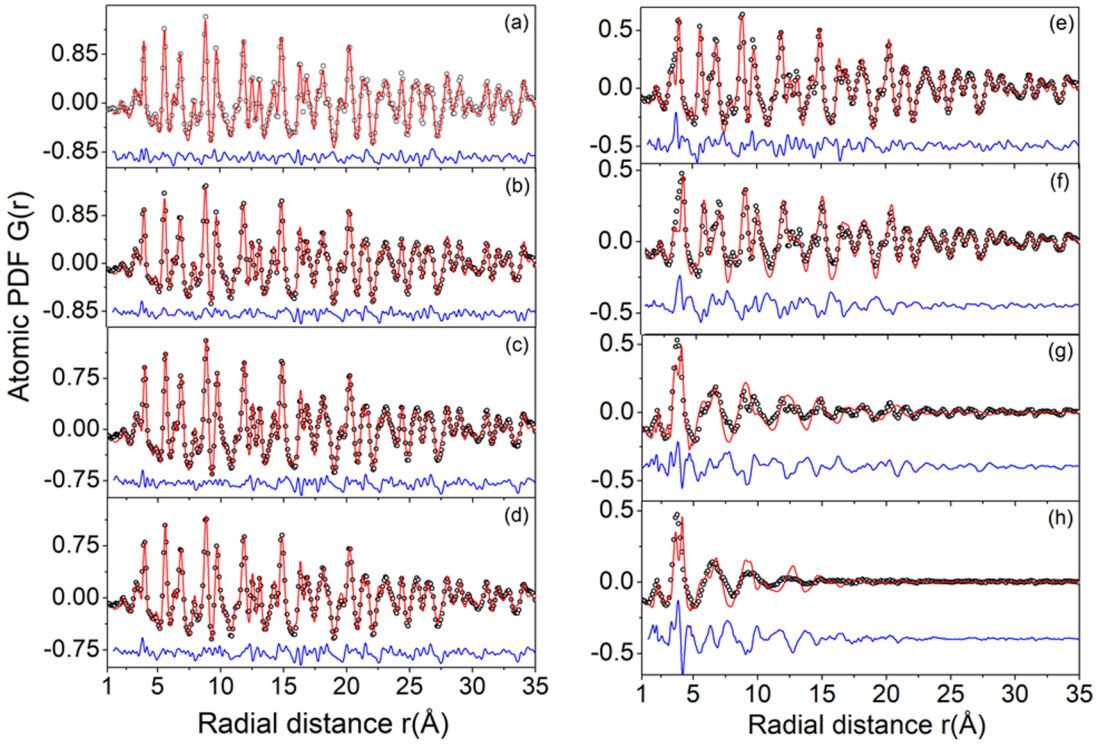

FIG. 6. Fits (red line) to experimental (symbols) atomic PDFs for (a) bulk $BiFeO_3$ and $BiFeO_3$ particles with a size of (b) 60 nm, (c) 29 nm, (d) 21 nm, (e) 19 nm, (f) 17 nm, (g) 14 nm, and (h) 10 nm. For clarity, the residual difference (blue line) is shifted downward by subtracting a constant. The fits are based on the rhombohedral (space group $R3c$) type structure exhibited by bulk $BiFeO_3$ at room temperature. The experimental PDFs for bulk $BiFeO_3$ and $BiFeO_3$ particles larger than 17 nm show well-resolved peaks, reflecting the presence of little local structural disorder. In addition, these PDF are well reproduced by the attempted rhombohedral model. Peaks in the PDFs for the particles with a size smaller than 19 nm appear much less resolved (e.g., see the PDF peak at about 4 Å), reflecting the increased presence of local structural disorder. In addition, they are not well reproduced by the attempted rhombohedral model. For reference, the values of the respective goodness-of-fit indicators are in the order of 30–40%, i.e., unacceptably high. These values are below 15% for the rhombohedral model fits to the PDFs of particles larger than 17 nm and bulk $BiFeO_3$.

The emergence of uncompensated Fe magnetic moments at the NP surface would also contribute to the increased magnetization. The presence of such moments, i.e., a ferromagnetic surface and antiferromagnetic core in the NPs, can explain the bifurcation of ZFC and FC curves for 60- and 29-nm BFO particles observed at low temperature.

As can be seen in Figs. 3, 9(b), and 9(c), both M_r, and H_c increase with diminishing particle size and peak when it becomes close to 19 nm, reflecting the emergence of a stable ferromagnetic order in BFO particles with a size between 19 and 62 nm. As can also be seen in Figs. 3, 9(b), and 9(c), M_r, and H_c start to decay steeply when the particle size decreases to 17 nm. One typical phenomenon related to finite size effects in systems exhibiting a ferromagnetic order is that its characteristic features, in particular M_r and H_c, would reach a maximum when the systems are reduced to a single-domain critical size, and then decay to zero when that size is decreased further. Concomitantly, the systems would exhibit a superparamagnetic behavior, where magnetization curves retain the ferromagnetic response but lose the loop, and M_s increases further with diminishing particle size. This is indeed the behavior exhibited by the magnetization curves for 17-, 14-, and 5-nm BFO particles shown in Fig. 3. The development of a maximum in the ZFC curves and its shift to lower temperatures with diminishing particle size (see the vertical arrows in Fig. 4) also indicate that the cooperative ferromagnetic order in BFO particles with a size below 17 nm disappears and they become superparamagnetic. In this regard, 17 nm may be considered as the critical limit for the disappearing of ferromagnetic order in BFO NPs.

Furthermore, the gradual weakening of superexchange antiferromagnetic interactions with diminishing particle size below 62 nm would result in an increased deviation of Fe-oxygen-Fe angles from 180°, i.e., increased antiferrodistortive rotations of Fe-oxygen octahedra and somewhat weakened ferroeletric order [51,54–60]. In ABO_3 perovskites, the magnitude of polyhedral rotation is related to their structural stability and size of A-type ions. The stability is often expressed in terms of the co-called tolerance factor t, where $t = (r_A + r_O)/\sqrt{2}(r_B + r_O)$ and r_A, r_B, and r_O are the ionic radii of metal (A/B) and oxygen atoms, respectively [61]. The tolerance factor for the ideal cubic perovskite shown in Fig. 1(a) is 1; it is 0.96 for $BiFeO_3$ and 1.06 for the archetypal ferroelectric perovskite $BaTiO_3$. The relatively low tolerance factor for $BiFeO_3$ is due to the fact that Bi ions are somewhat small ($r_{Bi} = 1.17$ Å) to fit tightly inside the cavities between oxygen octahedra, forcing the octahedra to rotate such that the volume of these cavities is reduced to match better the

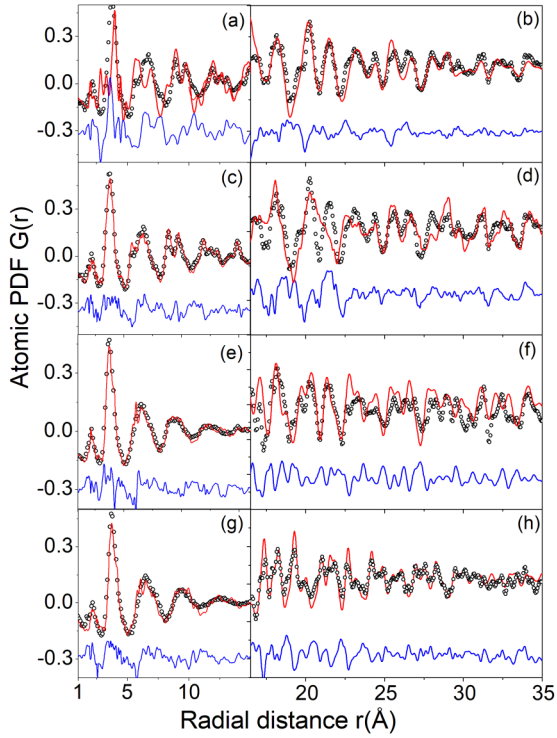

FIG. 7. Fits (red line) to experimental (symbols) atomic PDFs for $BiFeO_3$ particles with a size of (a)–(d) 14 nm, (e),(f) 10 nm, and (g),(h) 5 nm. For clarity, the residual difference (blue line) is shifted downward by subtracting a constant. The unsuccessful fit to the low-r PDF data for 14-nm particles shown in (a) is based on a cubic (space group Pm-3m) structure. The same structure model, however, reproduces very well the high-r PDF data for the same NPs shown in (b). The successful fit to the low-r PDF data for 10-nm particles shown in (c) is based on a distorted rhombohedral/trigonal (space group $P1$) structure. The same structure model, however, cannot reproduce the high-r PDF data for the same NPs shown in (d) as well as the cubic model shown in (b) does. The successful fit to the low-r PDF data for 10-nm particles shown in (e) is based on a distorted rhombohedral/trigonal (space group $P1$) structure and that to the high-r PDF data for the same particles shown in (f) on a cubic structure. The successful PDF fit in (g) is based on a distorted rhombohedral/trigonal (space group $P1$) structure and that in (h) on a cubic structure. Overall, data in the figure show that while the average structure of 14-, 10-, and 5-nm particles is cubic [as shown in (b), (f), and (h)], locally, they exhibit a distorted rhombohedral/trigonal structure [as shown in (c), (e), and (g)]. The structure features two distinct crystallographic sites for Fe atoms, which is in line with the findings of prior Moessbauer spectroscopy studies on 14-nm BFO NPs [34].

size of Bi atoms. This is not the case with the larger Ba ions ($r_{Ba} = 1.34$ Å), which fit tightly the cavities in the perovskite lattice of $BaTiO_3$ where no rotations of oxygen octahedra are observed. It may be expected that changes in the rotations in the Fe-oxygen octahedra in BFO NPs would change the positioning of Bi atoms in the cavities between them and, furthermore, these changes would not necessarily be the same for all Bi atoms in the NPs. This is because the crystal structure in NPs is more amenable to local structural fluctuations in comparison to the respective bulk. The effect would introduce

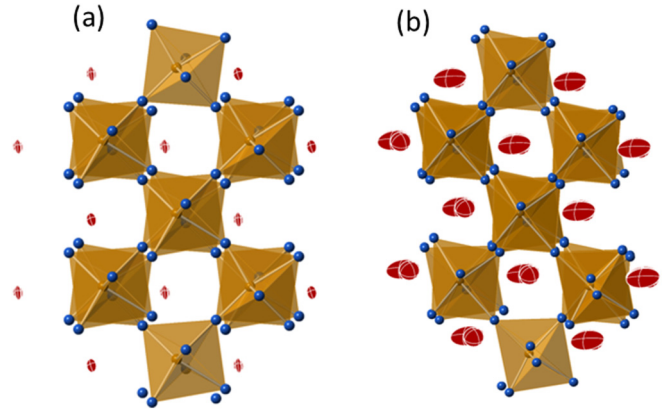

FIG. 8. Fragments from the structure of (a) bulk $BiFeO_3$ and (b) $BiFeO_3$ particles with a size of 10 nm, both of which have been refined against experimental PDF data as explained in the text. The rms displacements of Bi atoms are given as ellipsoids (red) positioned in between Fe-oxygen octahedra (brown). The displacements are very large in the nanoparticles in comparison to bulk BFO, reflecting the greatly increased atomic positional disorder in the Bi sublattice with diminishing particle's size.

fluctuations in the positions of Bi atoms in the oversized cavities between oxygen octahedra that are forced to undergo extra rotations due to diminished superexchange interactions. As such, the fluctuations would induce extra local structural disorder of a type similar to that introduced by heating (see Fig. 8). The emergence of such disorder is an effect exhibited by not only nanosized perovskites [62] but also semiconductor quantum dots and metallic nanoparticles [61,63–67]. Results of the PDF analysis conducted here (Tables S2–S5 [39] and Fig. 8) show that Bi atoms in BFO NPs with a size less than 19 nm suffer particularly strong positional disorder, as indicated by the sudden increase in their root-mean-square (rms) displacements. The displacements are likely to frustrate the long-range interactions between electric dipoles involving Bi atoms, leading to a destabilization of the long-range ferroelectric order and polar rhombohedral structure that favors it and, hence, stabilization of a nonpolar long-range structure of a cubic type, which is characteristic for paraelectric perovskites. As data in Figs. 9(e) and 9(f) show, both Fe-oxygen-Fe bond angles and rms displacements of Bi atoms undergo increasingly large changes when the size of BFO particles drops to 17 nm and below, and, at the same time, as the results of PDF analysis show, the average NP structure becomes cubiclike. Independent Raman studies have also indicated that cooperative lattice vibrations involving Bi atoms that control the ferroelectric order in BFO particles are strongly quenched when their size is reduced to 17 nm [57,68]. In this sense, the critical size R_c for ferroelectricity in BFO appears to be about 17 nm, i.e., twice the size suggested by data obtained by traditional crystallography techniques [36]. Moreover, it appears close to the critical size for ferroelectricity of 16 nm reported for $PbTiO_3$, indicating a common structural origin [69]. This may not come as a big surprise because the stereochemically active lone-pair electrons of A-type atoms in the ABO_3 perovskite lattice and related polar displacement of these atoms are known to largely generate the ferroelectricity

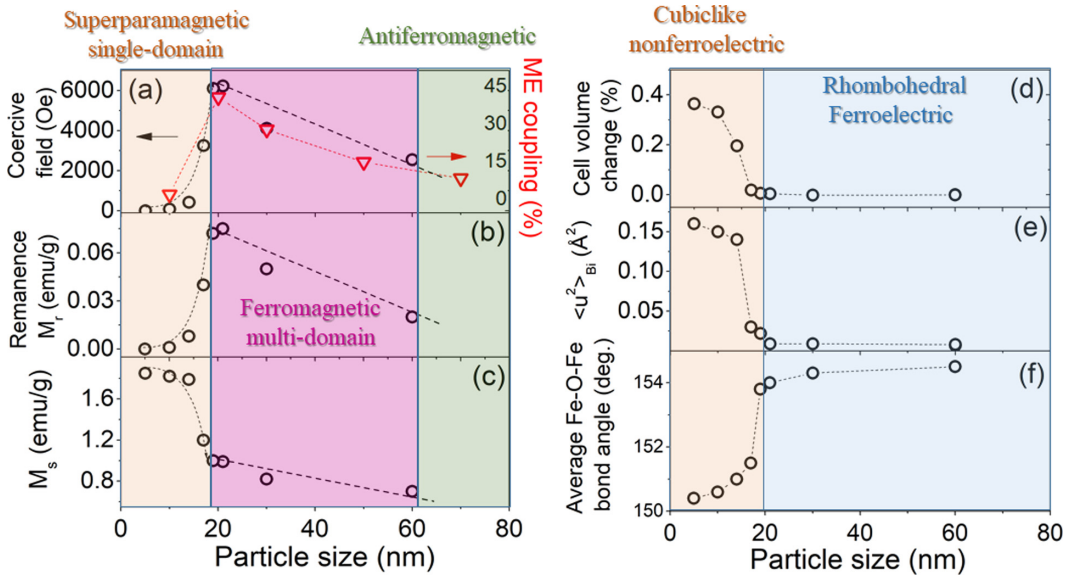

FIG. 9. (a) Coercive field, (b) remnant M_r, and (c) saturation M_s magnetization (at 9 T) derived from the experimental data for magnetization shown in Fig. 3. Also shown in (a) are experimental data for ME coupling reported in Refs. [51,73]. Data for the unit cell volume change, mean-square atomic displacements of Bi atoms, $\langle u^2 \rangle$, and average Fe-oxygen-Fe angle in $BiFeO_3$ nanoparticles shown in (d)–(f), respectively, are derived from fits to experimental PDFs shown in Figs. 6 and 7. All data sets in the figure show a similar, nonlinear evolution with particle size, indicating that they are interrelated. In particular, light brown area corresponds to BFO NPs that, on average, exhibit cubic structure, which is inconsistent with cooperative ferroelectricity, and also behave as single-domain superparamagnets. Light blue area corresponds to BFO NPs exhibiting a rhombohedral structure that sustains ferroelectricity. Light green area corresponds to BFO NPs that behave as bulk BFO, i.e., exhibit a rhombohedral structure and antiferromagnetic properties. Light magenta area corresponds to BFO NPs that are both ferromagnetic and ferroelectric, i.e., would exhibit an increased ME coupling.

in both $BiFeO_3$ and $PbTiO_3$. Notably, the unit cells of both nanosized $BiFeO_3$ [see Fig. 9(a)] and $PbTiO_3$ (see Fig. 3 in Ref. [69]) are found to expand markedly when R_c is reached upon diminishing particle size. An expanded perovskite lattice would allow larger rms displacements of Bi atoms, which, in turn, would weaken the covalent character of the Bi-O bond, thereby increasing its iconicity and short-range electrostatic repulsion between Bi and O ions favoring a high-symmetry cubic nanocrystal structure. The latter is consistent with the general observation that lattice expansion tends to promote an increase in the crystal symmetry [70]. Note that it is not uncommon for perovskites to exhibit local polar distortions and average nonpolar cubic structure due to temperature induced disordering, doping, and/or reduced particle size [69,71,72].

Evidently, the critical size for both ferroelectric and ferromagnetic orders in BFO NPs appears to be about 17 nm, i.e., the same, regardless of whether they arise from different mechanisms, where the former is driven by the lone-pair electrons of Bi and covalency of Bi-O bonds and the latter is caused by DM interactions that apparently prevail over the Fe-oxygen-Fe superexchange interactions when the spin cycloid is destroyed. Thus, it may be expected that the magnetoelectric coupling in BFO NPs would start to increase steadily when their size is diminished below 62 nm, i.e., when ferromagnetism emerges and both the local and average lattice structures are little disturbed and still polar. The increase will continue until their size approaches 19 nm, where the lattice structure starts to expand to accommodate the fast increasing positional disorder of Bi atoms and lose its polar character. It would then decay fast because both the long-range ferroelectric and ferromagnetic orders disappear with further diminishing particle's size, as described above. As can be seen in Fig. 9(a), experimental data for magnetoelectric coupling reported in Ref. [51] closely follow the evolution of structure and magnetic data obtained here, lending strong support to the scenario of a common critical size limit for ferroic orders in nanophase BFO.

V. CONCLUSION

Similarly to the prototype ferroelectric perovskite $PbTiO_3$, $BiFeO_3$ retains its polar crystallographic structure down to a particle size close to 19 nm. In particular, BFO NPs with a size in the range 19–60 nm retain the polar rhombohedral structure of the bulk state and can harbor ferroelectricity. In addition, the NPs appear ferromagnetic because of the destruction of the cycloidal and weakening of the antiferromagnetic orders, accompanied by the likely appearance of uncompensated magnetic moments at the NP surface. Thus, by reducing it to nanosized dimensions, $BiFeO_3$ can be brought to a state with an enhanced ME coupling that facilitates the mutual control between ferroelectric and magnetic degrees of freedom at room temperature, which is not possible in bulk BFO. On the other hand, BFO NPs with a size of 17 nm and smaller both acquire a nonpolar cubic structure, which is inconsistent with ferroelectricity, and lose their ferromagnetic properties simultaneously. The ferroelectric order seems to disappear largely because of the increased positional disorder of Bi atoms and resulting disruption of the interactions

between Bi-involving electric dipoles that are known to stabilize their arrangement in a long-range ordered pattern. The ferromagnetic order disappears likely because, in general, an increase in the lattice symmetry leads to a decrease in the magnetocrystalline anisotropy energy, which is known to induce superparamagnetic behavior in sufficiently small nanoparticles. Thus, the observed decrease of the local lattice symmetry to triclinic due to Bi atoms disordering and the increase of the average lattice symmetry from rhombohedral to cubic coupled to a rather steep lattice expansion taking place in nanosized $BiFeO_3$ seem to be promoted by the concurrent disappearance of ferroelectric and ferromagnetic orders, and vice versa. This is a rare example of interactions between lattice, ferroelectric, and magnetic degrees of freedom at the nanoscale that determine the particle size range for coexistence and critical particle size limit for existence of ferroic orders in perovskites.

ACKNOWLEDGMENTS

This work was supported by the U.S. Department of Energy, Office of Science, Office of Basic Energy Sciences under Award No. DE-SC0021973 and used resources of the Advanced Photon Source at the Argonne National Laboratory provided by the DOE Office of Science under Contract No. DE-AC02-06CH11357. Thanks are due to K. Chapagain for the help with magnetic measurements.

[1] M. Fiebig, Th. Lottermoser, and M. Trassin, Nat. Rev. Mater. **1**, 16046 (2016).
[2] D. Khomskii, Physics **2**, 20 (2009).
[3] R. Ramesh and N. A. Spaldin, Nat. Mater. **6**, 21 (2007).
[4] S. W. Cheong and M. Mostovov, Nat. Mater. **6**, 13 (2007).
[5] N. Spaldin, S.-W. Cheong, and R. Ramesh, Phys. Today **63**(10) (2010).
[6] M. Gajek, M. Bibes, S. Fusil, K. Bouzehouane, J. Fontcuberta, A. Barthelemy, and A. Fert, Nat. Mater. **6**, 296 (2007).
[7] C.-W. Nan, J. Appl. Phys. **103**, 031101 (2008).
[8] Ch. Binek and B. Doudin, J. Phys.: Condens. Matter **17**, L39 (2004).
[9] A. Cavalleri, R. Merlin, A. V. Kimel, R. V. Mikhaylovskiy, D. Bossini, M. Först, A. Cantaluppi, A. Cartella, and T. F. Nova, Nat. Phys. **13**, 132 (2017).
[10] J. T. Han, Y.-H. Huang, X.-J. Wu, C.-L. Wu, W. Wei, B. Peng, W. Huang, and J. B. Goodenough, Adv. Mater. **18**, 2145 (2006).
[11] S. V. Kiselev, R. P. Ozerov, and G. S. Zhdanov, Sov. Phys. Dokl. **7**, 742 (1963).
[12] I. H. Lone, J. Aslam, N. R. E. Radwan, A. H. Bashal, A. F. Ajlou, and A. Ajhter, Nano Res. Lett. **14**, 142 (2019).
[13] Y. Yin and Q. Li, J. Materiomics **3**, 245 (2017).
[14] J. Silav, A. Reyes, H. Esparza, H. Camacho, and L. Fuentes, Integrated Ferro. **126**, 47 (2011).
[15] A. Palewicza, I. Sosnowska, R. Przeniosło, and A. W. Hewat, Acta Phys. Pol. A **117**, 296 (2010).
[16] U. Nuraini and S. Suasmoro, J. Phys.: Conf. Ser. **817**, 012059 (2017).
[17] H. D. Megaw and C. N. W. Darlington, Acta Crystallogr., Sect. A **31**, 161 (1975).
[18] O. Dieguez, O. E. Gonzalez-Vazquez, J. C. Wojdel, and J. Iniguez, Phys. Rev. B **83**, 094105 (2011).
[19] A. Palewicz, P. Rrzenioslo, I. Sosonowska, and A. W. Hewat, Acta Crystallogr., Sect. B **63**, 537 (2007).
[20] R. Saeterli, S. M. Selbah, P. Ravindran, T. Grande, and R. Holmestad, Phys. Rev. B **82**, 064102 (2010).
[21] D. Ricinschi, K.-Y. Yun, and M. Okuyama, J. Phys.: Condens. Matter **18**, L97 (2006).
[22] I.-T. Bae, A. Kovacs, H. J. Zhao, J. Iniguez, Sh. Yasui, T. Ichinose, and H. Naganuma, Sci. Rep. **7**, 46498 (2017).
[23] I. Sosowska, T. P. Neumaier, and E. Steichele, J. Phys. C: Solid State Phys. **15**, 4835 (1982).
[24] Y. Hong, J. Li, H. Bai, Z. Song, and M. Wang, Zh. J. Adv. Ceram. **9**, 641 ((2020).
[25] A. J. Jacobson and B. E. F. Fender, J. Phys. C: Solid State Phys. **8**, 844 (1975).
[26] N. V. Shrihari, K. B. Vinayakumar, and K. K. Nagaraja, Coatings **10**, 1221 (2020).
[27] S. Kawachi, S. Miyahara, T. Ito, A. Miyake, N. Furukawa, J. I. Yamaura, and M. Tokunaga, Phys. Rev. B **100**, 140412 (2019).
[28] A. Agbelele, D. Sando, C. Toulouse, C. Paillard, R. D. Johnson, R. Rüffer, A. F. Popkov, C. Carrétéro, P. Rovillain, J.-M. Le Breton, B. Dkhil, M. Cazayous, Y. Gallais, M.-A. Méasson, A. Sacuto, P. Manuel, A. K. Zvezdin, A. Barthélémy, J. Juraszek, and M. Bibes, Adv. Mater. **29**, 1602327 (2017).
[29] M. D. Davydova, K. A. Zvezdin, A. A. Mukhin, and A. K. Zvezdin, Phys. Sci. Rev. **5**, 20190070 (2020).
[30] E. Ramos, A. Cardona-Rodriguez, D. Carranza-Celis, R. Gonzales-Hernandes, D. Muraca, and J. G. Ramirez, J. Phys.: Condens. Matter **32**, 185703 (2020).
[31] N. Wang, X. Luo, L. Han, Zh. Zhang, R. Zhang, H. Olin, and Ya Yang, Nano-Micro Lett. **12**, 81 (2020).
[32] V. A. Reddy, N. P. Pathak, and R. Nath, J. Alloys Compd. **543**, 206 (2012).
[33] R. Mazumder, S. Ghosh, P. Mondal, D. Bhattacharya, S. Dasgupta, N. Das, and A. Sen, J. App. Phys. **100**, 033908 (2006).
[34] T.-J. Park, G. C. Papaefthymiou, A. J. Viescas, A. R. Moodenbaugh, and S. Wong, Nano Lett. **7**, 766 (2007).
[35] F. Huang, Zh. Wang, X. Lu, J. Zhang, K. Min, W. Lin, R. Ti, T. Xu, Ch. Yue, and J. Zhu, Sci. Rep. **3**, 2907 (2013).
[36] S. M. Selbach, Th. Tybell, M.-A. Einarsrud, and T. Grande, Chem. Phys. **19**, 6478 (2007).
[37] D. Carranza-Celis, A. Cordona-Rodriguez, J. Narvaez, O. Moscoso-londono, D. Muraca, M. Knobel, N. Ornelas-Soto, A. Reiber, and G. Ramirez, Sci. Rep. **9**, 3182 (2019).
[38] Occasionally, TEM estimated particles size may appear larger than the XRD estimated one because a single particle may contain a few misoriented crystallites.
[39] See Supplemental Material at http://link.aps.org/supplemental/10.1103/PhysRevB.104.054121 for TEM image and results from fits to experimental XRD patterns and atomic PDFs.
[40] V. Petkov, S. M. Selbach, M.-A. Einarsrud, T. Grande, and S. D. Shastri, Phys. Rev. Lett. **105**, 185501 (2010).
[41] V. Petkov, J. Appl. Crystallogr. **22**, 387 (1989).

[42] B. H. Toby and R. B. Von Dreele, J. Appl. Crystallogr. **46**, 544 (2013).
[43] S. C. Abrahams, S. K. Kurtz, and P. B. Jamieson, Phys. Rev. **172**, 551 (1968).
[44] J. B. Neaton, C. Ederer, U. V. Waghmare, N. A. Spaldin, and K. M. Rabe, Phys. Rev. B **71**, 014113 (2005).
[45] S. Tsunekawa, S. Ito, T. Mori, K. Ishikawa, Z.-Q. Li, and Y. Kawazoe, Phys. Rev. B **62**, 3065 (2000).
[46] D. Lebeugle, D. Colson, A. Forget, and M. Viret, Appl. Phys. Lett. **91**, 022907 (2007).
[47] Y. Jin, X. Lu, J. Zhang, Y. Kan, H. Bo, F. Huang, T. Xu, Y. Du, Sh. Xiao, and J. Zho, Sci. Rep. **5**, 12237 (2015).
[48] T. Egami and S. J. L. Billinge, Underneath the Bragg peaks, *Structural Analysis of Complex Materials* (Pergamon, Oxford, UK, 2003).
[49] V. Petkov, *Characterization of Materials* (John Wiley & Sons, New York, 2003).
[50] H. Wang, Ch. Yang, J. Lu, M. Wu, J. Su, K. Lin, J. Zh, G. Li, T. Jin, T. Kamiyama, F. Liao, J. Lin, and Y. Wu, Inorg. Chem. **52**, 2388 (2013).
[51] S. Goswami, D. Bhattacharya, Ch. K. Ghosh, B. Ghosh, S. D. Kaushik, V. Sirugui, and S. R. P. Krishna, Sci. Rep. **8**, 3728 (2018).
[52] S. Vijayanand, M. B. Mahajan, H. S. Potdar, and P. A. Joy, Phys. Rev. B **80**, 064423 (2009).
[53] S. Nakamura, S. Soeya, N. Ikeda, and M. Tanaka, J. Appl. Phys. **74**, 5652 (1993).
[54] S. Goswami, A. sahoo, D. Bhattacharya, O. Karci, and P. K. Mohanty, APL Mater. **8**, 081101 (2020).
[55] M. K. Singh, R. S. Katiyar, and J. F. Scott, J. Phys.: Condens. Matter **20**, 252203 (2008).
[56] M. j. K. Singh, S. Dussan, W. Prellier, and R. S. Katiyar, J. Magn. Magn. Mater. **321**, 1706 (2009).
[57] A. Jaiswal, R. Das, T. Maity, K. Vivekan, S. Adyanthaya, and P. Poddar, J. Phys. Chem. **114**, 12432 (2010).
[58] V. M. Gaikwad and S. A. Acharaya, Adv. Mater. Lett. **5**, 157 (2014).
[59] Jr. Brown and F. William, Phys. Rev. **130**, 1677 (1963).
[60] T.-J. Park, Sh. Sambasivan, D. A. Fischer, W.-S. Yoon, J. A. Misewich, and S. S. Wong, J. Phys. Chem. C **112**, 10359 (2008).
[61] X. Liu, R. Hong, and Ch. Tian, J. Mater. Sci.: Mater. Electron. **20**, 323 (2009).
[62] K. Page, Th. Proffen, M. Niederberger, and R. Seshadri, Chem. Mater. **22**, 4386 (2010).
[63] T. Zhao, A. Scholl, F. Zavaliche, K. Lee, M. Barry, A. Dogan, M. P. Cruz, Y. H. Chu, C. Ederer, N. A. Spaldin, R. R. Das, D. M. Kim, S. H. Baek, C. B. Eom, and R. Ramesh, Nat. Mater. **5**, 823 (2006).
[64] D. Lebeugle, M. Viret, D. Colson, and L. Ranno, Phys. Rev. Lett. **103**, 257601 (2009).
[65] V. Petkov, N. Bedford, M. R. Knecht, M. G. Weir, R. M. Crooks, W. Tang, G. Henkelman, and A. Frenkel, J. Phys. Chem. C **112**, 8907 (2008).
[66] B. Gilbert, F. Huang, H. Zhang, G. A. Waychunas, and F. J. Banfield, Science **305**, 651 (2004).
[67] E. M. Janke, N. E. Williams, Ch. She, D. Zherebetskyy, M. H. Hudson, L. Wang, D. J. Gosztola, R. D. Schaller, B. Lee, Ch. Sun, G. S. Engel, and D. V. Talapin, J. Am Chem. Soc. **140**, 15791 (2018).
[68] G. Catalan and J. F. Scott, Adv. Mater. **21**, 2463 (2009).
[69] E. K. Akdogan, C. J. Rawn, W. D. Porter, and E. A. Payzant, J. Appl. Phys. **97**, 084305 (2005).
[70] S. K. Filatov, Cryst. Rep. **56**, 953 (2011).
[71] S. Schlag and H.-F. Eicke, Solid State Commun. **91**, 883 (1994).
[72] V. Petkov and V. Buscaglia, Phys. Rev. Materials **5**, 044410 (2021).
[73] The data for ME coupling shown in Fig. 9(a) are shifted to the left by about 10 nm in comparison to their values reported in Fig. 6(d) in Ref. [51] to account for the fact that a particle size determined by XRD, as done here, is typically smaller than that determined by TEM, as done in Ref. [51]. The shift does not change the observed specific dependence of ME coupling in BFO NPs on their size.